Magnetic Shielding of Solenoid-Based Focusing Lenses
for Superconducting Sections of HINS Linac

G. Davis, C. Hess, Y. Huang, F. Lewis, T. Nicol, D. Orris, R. Rabehl, S. Sanchez,
D. Sergatskov, M. Tartaglia, I. Terechkine, J. Tompkins, T. Wokas

I. Introduction

Low energy sections of HINS linac use superconducting solenoids as focusing lenses for H$^-$ beam transverse confinement. The solenoids ought to generate quite high magnetic field (up to 7 T) to provide needed focusing. Because the solenoids are installed between accelerating superconducting cavities, the problem exists of reducing fringe field of the solenoids to a level that does not compromise performance of the cavities. Effect of the fringe field was studied in [1]: the main result of this work was understanding the allowed level of the magnetic field on walls of 325 MHz spoke cavities. The main criterion of the cavity performance was its quality factor, which was allowed to drop by a factor of two if the cavity temperature is 2K (expected residual resistance R_s=20 nOhm). It was found in this case that the average stray magnetic field on the walls must be below 10 µT (the typical level of the Earth magnetic field is ~100 µT or 1 G). Although this requirement is much looser than the initial one (1 µT), still the required stray field is quite low, and it is difficult to verify that this condition is met. At 4.2 K, the average 10 µT magnetic field corresponds to ~30% of the cavity quality factor drop.

Two main sources of magnetic field exist inside the cryomodules that contain superconducting RF cavities: the magnetic field of the Earth and stray magnetic field of the focusing lenses. The cryostat is equipped with a magnetic shield that reduces the level of the Earth magnetic field. Although design measures (using bucking coils and a flux clamp) were taken to greatly reduce the field outside the solenoids, still the stray field level is on the order of several Gauss, and additional magnetic shielding is necessary. Therefore a shield was designed [2] and fabricated of Cryoperm10®, which has high permeability at 4 K, to meet the fringe field requirement.

To measure performance of the magnetic shield, the Test Cryostat made for SRF cavity testing [3] was used. The cryostat became available for this study because of some delay in the cavity readiness for testing. Some modifications to the Test Cryostat were made to allow cryogenic operation and powering of the SS1 prototype focusing solenoid, which had previously been tested [4], and dedicated sensors and instrumentation were configured to measure stray magnetic field of the shielded solenoid.

The primary purpose of this note is to discuss the design and performance of the SS1 solenoid magnetic shielding. However, a great deal has been learned about the Test Cryostat design and performance, from both a magnetic and cryogenic operation perspective; therefore, we include details and results about these aspects as well.

II. Test Cryostat Magnetic Shield

The magnetic shield of an RF cryomodule protects superconducting cavities mounted inside the cryomodule from the magnetic field of Earth, which otherwise would result in the cavity performance degradation. For the Test Cryostat [3] the shield was made of Amumetal® (type of mu-metal developed by Amuneal, Inc.) and installed between the

vacuum vessel and thermal shield inside the cryostat. A photo of the Test Cryostat in Fig. II.1 shows the magnetic shield inside the end dome.

Fig. II.1. Test Cryostat with open end showing Earth magnetic shield.

Performance of the shield was measured at room temperature after the vessel was assembled. A Flux Gate magnetometer was used to measure the magnitude of the field as a function of position in the volume where the cavity will reside. The Earth magnetic field without the shielding was found to be ~0.75 G (75 μT). Fig. II.2 shows the measured field inside the cryostat versus vertical distance from the plane of the cryostat top flange (see Fig. II.1): 0.5 m corresponds to the center of the cryostat. Four sets of measurements were made at 90-degree intervals around the inner diameter of the top flange opening (Ø ~ 400 mm). The measurements showed that in the central region of the cryostat the room temperature magnetic field is below 0.04 G (4 μT), which is below the required 10 μT level.

Amumetal® is Ni-Co-Fe alloy that has very high permeability at 300 K (up to 80000) if annealed properly. At temperature below ~100 K, this material's permeability becomes significantly lower, and Cryoperm10® is usually used. Fig. II.3 compares performance of the two materials.

During the cold test of the solenoid magnetic shield, the LN2 thermal shield operated at about 100 K, which is close to optimal temperature. The cryostat magnetic shield temperature was not measured; because the shield was located between the LN2 shield and the vacuum vessel walls with MLI insulation separating it from the LN2 shield, this temperature should be very close to that of the vessel.
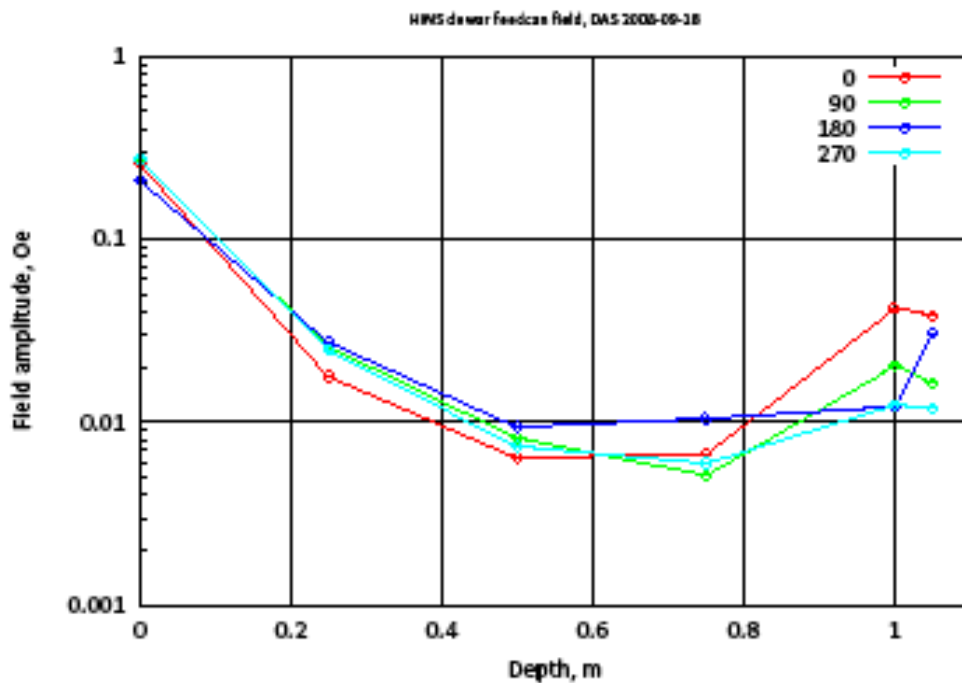
Fig. II.2. Room temperature background magnetic field inside the Test Cryostat with Amuneal shield installed.
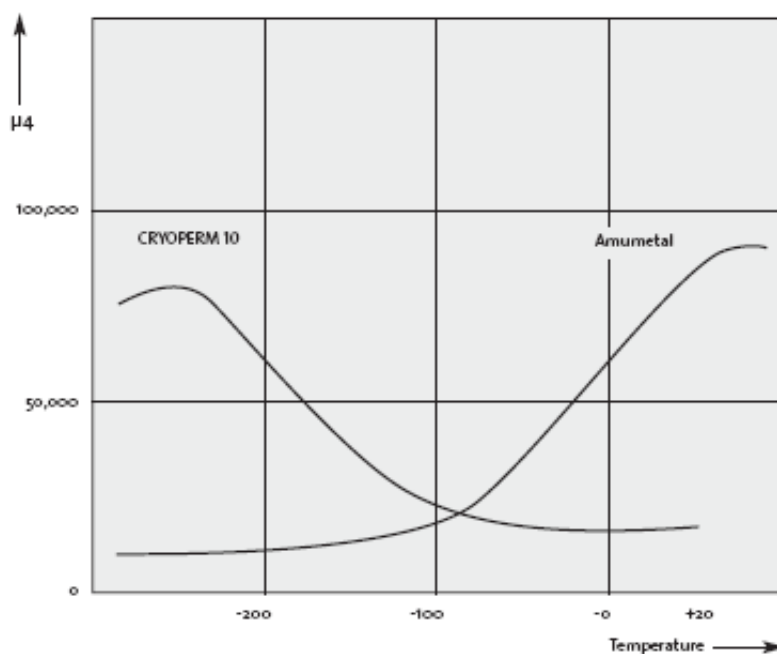

Fig. II.3. Permeability of Cryoperm10® and Amumetal® as a function of temperature in degrees Centigrade (from the Amuneal, Inc. data sheet).

III. Solenoid Magnetic Shield Design

Magnetic properties of both Cryoperm10® and Amumetal® strongly depend not only on temperature, but on the annealing process and are very sensitive to stress. While the annealing regimes are easily reproducible, handling of the material is always a concern. The HINS cryostat assembly process is not yet well defined, and it was important to understand restrictions that the magnetic shielding would bring to the cryomodule assembly process. It was also important to obtain a definite answer to the question of whether the magnetic shielding works as desired in an environment close to what is expected in HINS cryomodules. Using two different approximations for the non-linear behavior of the flux return material - magnetic properties of which are quite uncertain - results of modeling were slightly different, although both satisfied the requirements. This added a certain level of doubt in our ability to rely on modeling alone. The most direct way to get a definitive answer was to use the temporarily available Test Cryostat to conduct R&D with the following scope:

1. Find a design solution for the magnetic shield
2. Modify the test cryostat to accommodate the focusing solenoid
3. Develop a scheme for the low field measurements in cryogenic environment (vacuum and low temperature) and build the measurement setup
4. Test performance of the prototype solenoid and Test Cryostat under realistic operating conditions
5. Measure the fringe field of the solenoid and the dipole correctors with installed magnetic shield at the location of RF cavity wall.

In the first design iteration, simple 2D and 3D models of a magnetic shield were built. The shield consisted of three parts: a cylinder and two end walls, all made of 1-mm ferromagnetic sheet material with permeability $\mu=10^4$ and connected to each other without gaps. The cylinder with ID=300 mm did not have any holes. The front and back walls were placed 150 mm from the center of the solenoid; they had 40 mm diameter holes for the beam pipe. Fig. III.1 compares the fringe magnetic field of the SS1 focusing lens in [4] for the cases with and without the shield in the plane Z = 225 mm, where superconducting cavity walls are to be placed.
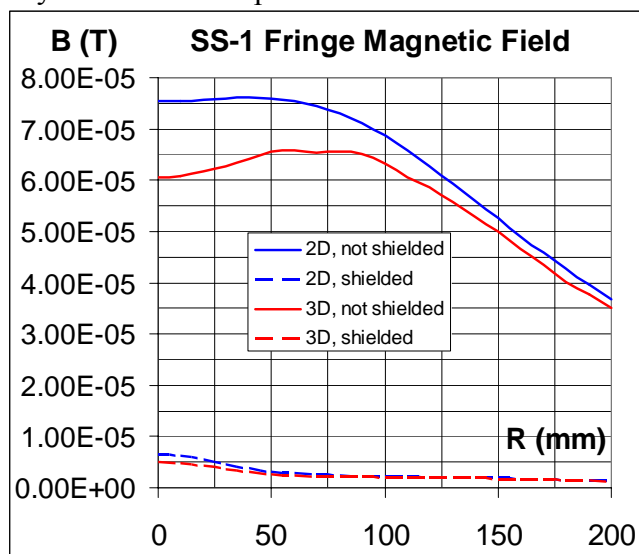

Fig. III.1. Comparison of modeled magnetic shielding effectiveness for 2D and 3D cases.

The results of 2D and 3D modeling are quite comparable: both models show that the additional shielding is definitely needed. Because the shield must have holes for LHe pipe, support post, alignment elements, and current leads, a 3D model must be used to analyze the actual shield design. The 2D design is adequate to study the sensitivity of fringe field (radial and azimuthal components) to various parameters, such as the permeability, and distance of the shield end walls and cavity walls from the center of the solenoid. This kind of an independent 2D model study was made; the results were in agreement with the results obtained by 3-D modeling.

Holes in the shield result in some magnetic flux leakage. One way to reduce the magnetic field penetration through a hole in the radial wall is to use flux catchers made as cylinders attached to the hole bases. Fig. III.2 shows a comparison of different cases with and without the flux catcher, at a solenoid current of 200 A. Here the absolute value of the field strength is plotted as a function of the radial distance from the hole center at the Z = 225 mm position (Z is the distance from the solenoid center). Increasing the opening diameter results in a significant fringe field rise. Flux catchers help to reduce the field near the axis, but may not help much in the peripheral area. Increasing permeability helps to reduce the fringe field everywhere.
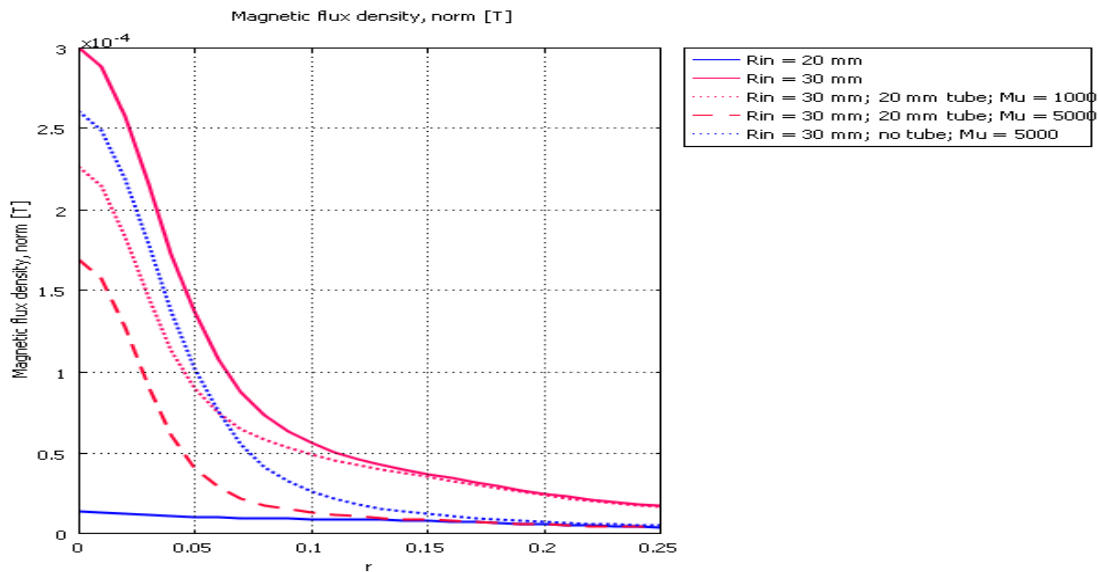

Fig. III.2. Effect of flux catchers, hole diameter, and material permeability (Mu) on the magnetic field along the radial wall of the shield.

The magnetic shield will be assembled in the cryomodule after installation of all other major parts, so it must be made of several pieces and take into account piping associated with the LHe vessel of the lens. A schematic layout of one cell of the cryomodule is shown in Fig. III.3. Introducing flux catchers significantly complicates assembly of the shield and requires additional space in the cryomodule, whereas space for cavity placement is already quite limited. So an effort was made to develop a design that does not employ them.
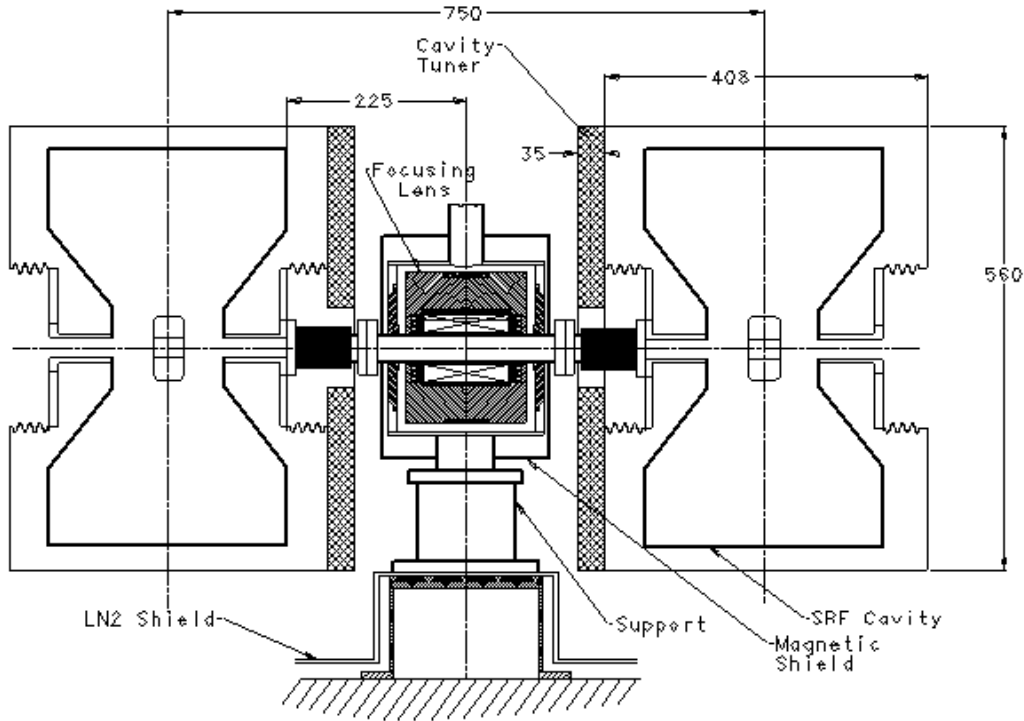
Fig. III.3. Placement of SS1 focusing lens between two SRF cavities.

A box-type shield was designed, similar in size to the original cylindrical model. The box was made of 1-mm Cryoperm10® plates (assumed $\mu=10^4$) that are tightly connected to each other. To accommodate the beam pipe, two 40 mm diameter holes were made in the end plates located at Z = 150 mm. No other holes were made during the first iteration of the analysis, and no flux catchers were used. Fig. III.4 compares magnetic field strength versus radial distance in the transverse planes at Z = 200 mm and Z = 230 mm.
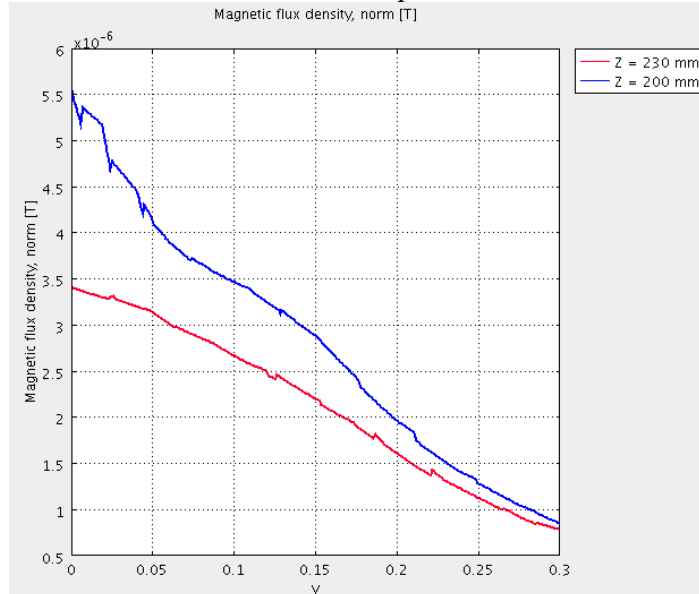

Fig. III.4. Magnetic field in the planes at Z = 200 mm and Z = 230 mm with first iteration box-type shield.

In this (nearly ideal) case, the field on the walls of the cavity does not exceed 3 μT. This result is comparable to that in Fig. III.1, and the field requirements are met. This allowed us to gradually introduce in the model other features that can increase the fringe field, like possible gaps between the plates and holes needed for different features of the lens and its LHe vessel. These features were introduced sequentially to see how each of them changes the fringe field environment. First, a 100 mm diameter hole in the bottom plate and 50 mm dia. hole in the top plate were introduced to conclude that, although the local magnetic field changes dramatically, little change occurs in the plane Z = 225 mm where the cavity wall is located. Adding a 75-mm hole in the bottom of the side wall also adds just small fraction to the fringe field. There are two alignment beams attached to the LHe vessel that penetrate the shield. These beams are 5 mm wide and 50 mm high; 10 mm x 60 mm cuts are made on both side plates of the shield for the beams. The resultant fringe field increase is quite modest. Finally, gaps between the plates were introduced. The gaps interrupt flux lines inside the shield, and can significantly compromise the fringe field. If the gaps are managed in a way that increases the area for flux crossing (e.g., by using 20 mm overlapping flaps), the fringe field can be brought back to the acceptable limit. Fig. III.5 below shows the final 3D model with the magnetic field mapped in several planes, including the plane Z = 230 mm. To simplify the model, only 1/8 of the total assembly was used with proper symmetry conditions applied; this resulted in having more (and bigger) holes in the shield than it is expected in reality. With 20 μm gaps between the plates and 20 mm flaps, the field in this plane does not exceed 6 μT.
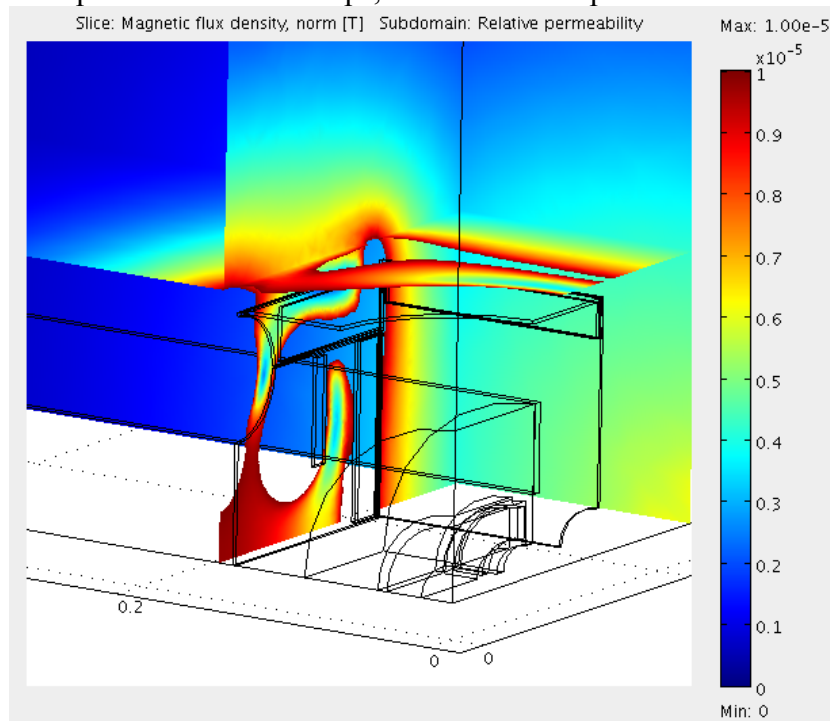

Fig. III.5. Magnetic field outside the magnetic shield at I = 200 A.

Having acceptable magnetic shield modeling results, the design was made and the shield was fabricated at Amuneal, Inc. The design drawings are shown in Fig. III.6. One issue with the design was found during the shield assembly around the solenoid at Fermilab: the top plate could not be installed around the helium pipes because of a larger

diameter flange at the interconnect to the helium supply lines. It was necessary to modify this part by cutting it for the test fit. Since stresses can change the material properties, this part was returned to the vendor; it was redesigned as a two-piece unit with batten plates, similar to the end plates, and was re-annealed. After assembly, the shield was wrapped in a blanket of super-insulation, and mounted inside the Test Cryostat, with a Hall probe array positioned 225 mm from the solenoid center. Figure III.7 shows photos of the magnetic shield assembly with the top plate removed for modification, and as first installed in the cryostat.
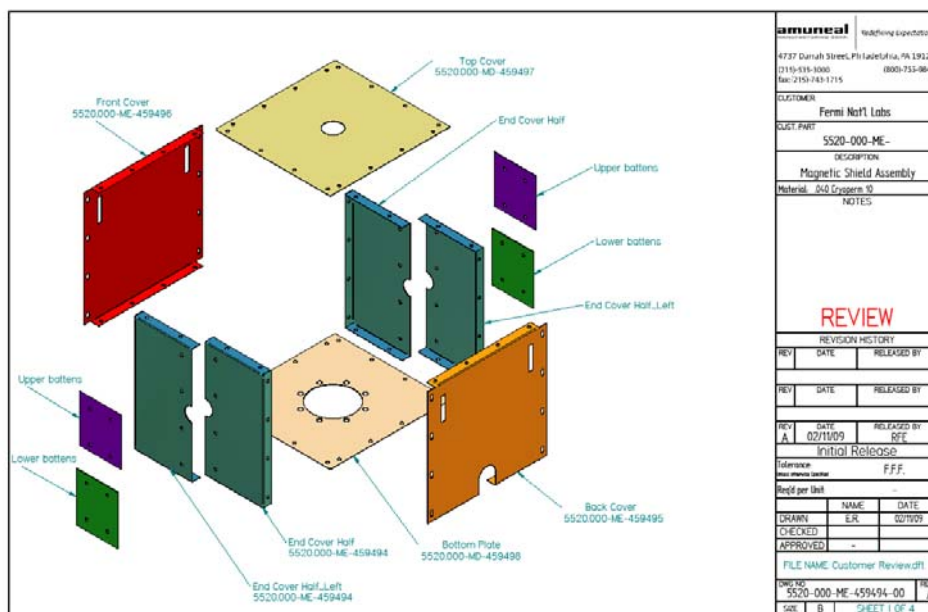

Fig. III.6. Magnetic shield design by Amuneal, Inc.

Fig. III.7. Assembled magnetic shield (without top plate) and installed with insulation.

IV. Test Cryostat

The design of the Test Cryostat has been described in detail elsewhere [3]. In this section, we discuss the modifications made to adapt the Test Cryostat for powering the SS1 solenoid at liquid helium temperature.

Current leads and Superconducting Bus

Six vapor-cooled 300A copper current leads were used to power the solenoid and the correctors of the lens. The superconducting (S/C) bus connections to the coils were made from 0.8 mm NbTi strand soldered to a 10 mm^2 solid copper stabilizer. Protection and monitoring voltage taps were placed at the top and bottom of each copper lead, and at the splice between the solenoid and S/C bus leads. In order to limit the number of required taps from the helium space, each correction dipole and its two S/C leads were protected as one low inductance circuit using taps at the bottom of the copper leads. Voltage tap wires were routed through a tube in the center of the current lead stack, to a Stycast®-potted connector. Figure IV.1 shows the early assembly with stabilized S/C attached to copper leads, and late assembly with helium jacket and insulated S/C bus, before insertion into insulating vacuum sleeve and helium tube for connection to the solenoid.
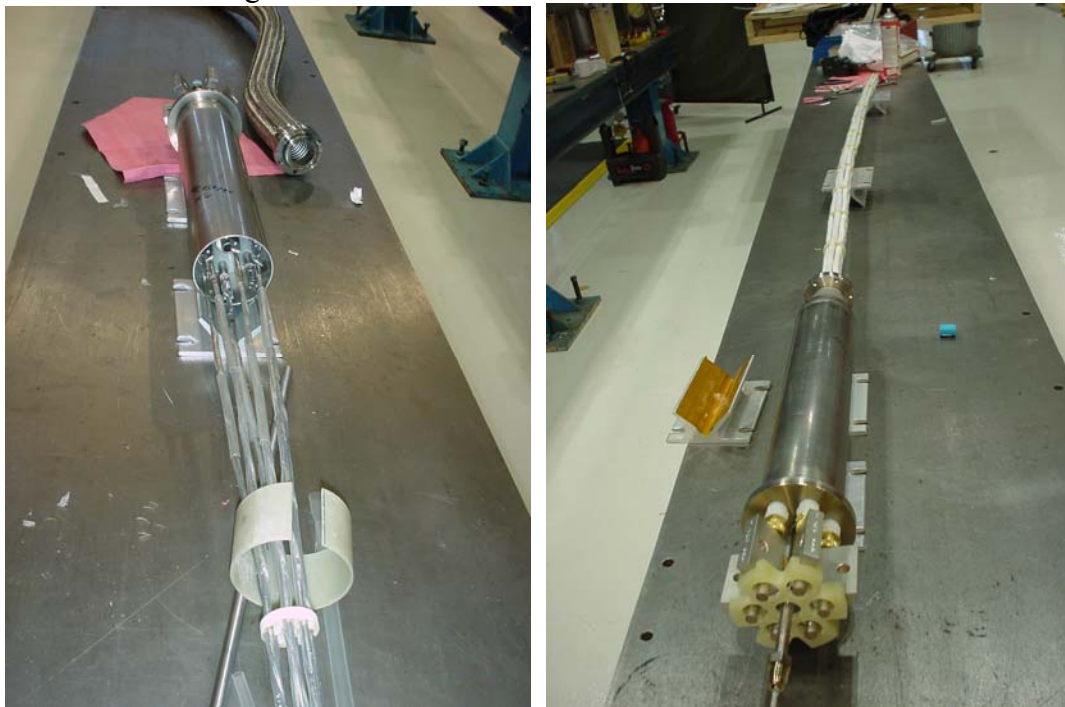

Fig. IV.1. Early (left) and late (right) assembly stages of vapor-cooled leads.

Proximity of the current leads to the RF cavity walls should also be considered as a source of stray field, and additional shielding of the leads is probably needed in the production cryostat. An upper limit on the power leads contribution to the magnetic field can be estimated knowing their distance to the Hall probe array, with a reasonable assumption about the separation of the leads. Figure IV.2 shows a detail of the splice, and Fig. IV.3 shows that the Hall probes are about 30 cm from any unshielded section of the leads where they are spliced. Assuming a 1 cm separation could result in a field as high as 2 μT at 175 A.
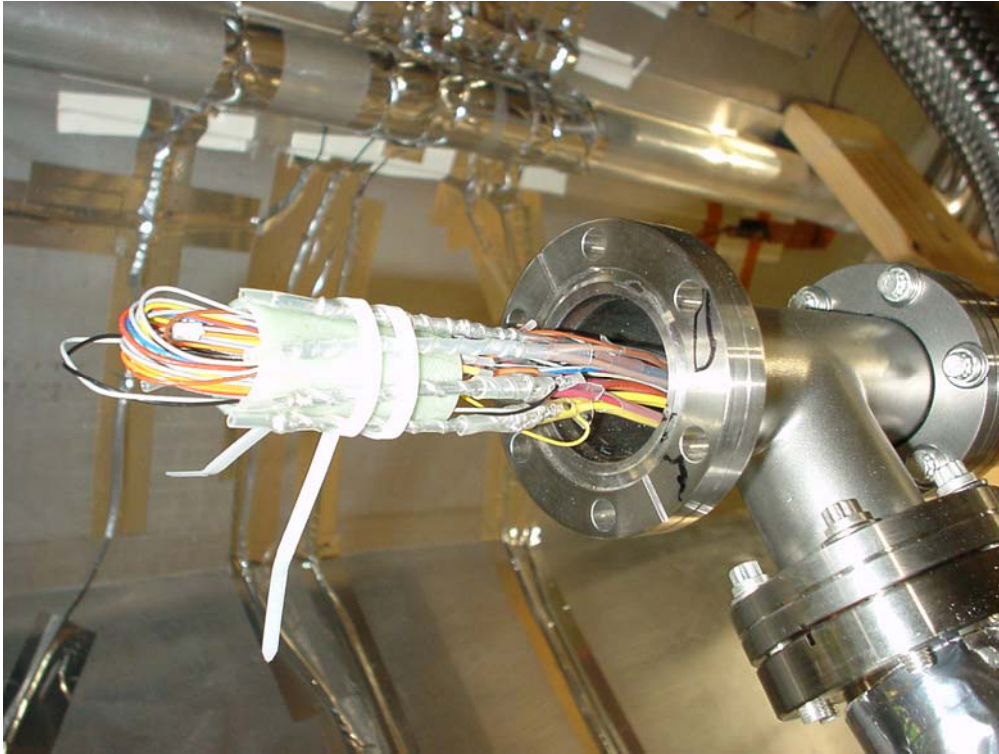
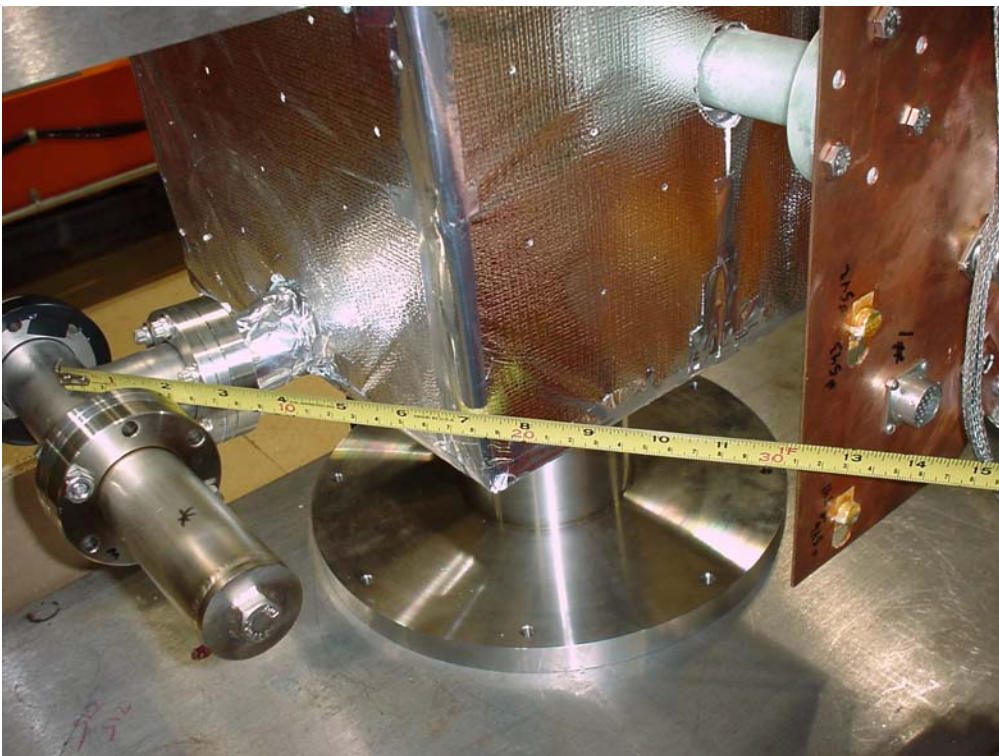Fig. IV.2. Detail of splices and voltage taps between Sc Leads and coils.

Fig. IV.3. Geometry of Sc Leads and splice with respect to Hall probe array.

Internal Piping

The prototype focusing lens in [4] was first welded into a helium vessel, and equipped with the magnetic shield described above, then mounted on the post inside the cryostat. In contrast to the flow diagram for cavity testing (Fig. 7 in [3]), the helium supply was connected directly to the solenoid from the phase separator, and the helium return was taken from the current lead flows. Fig. IV.4 shows the internal piping assembly as received from the vendor.
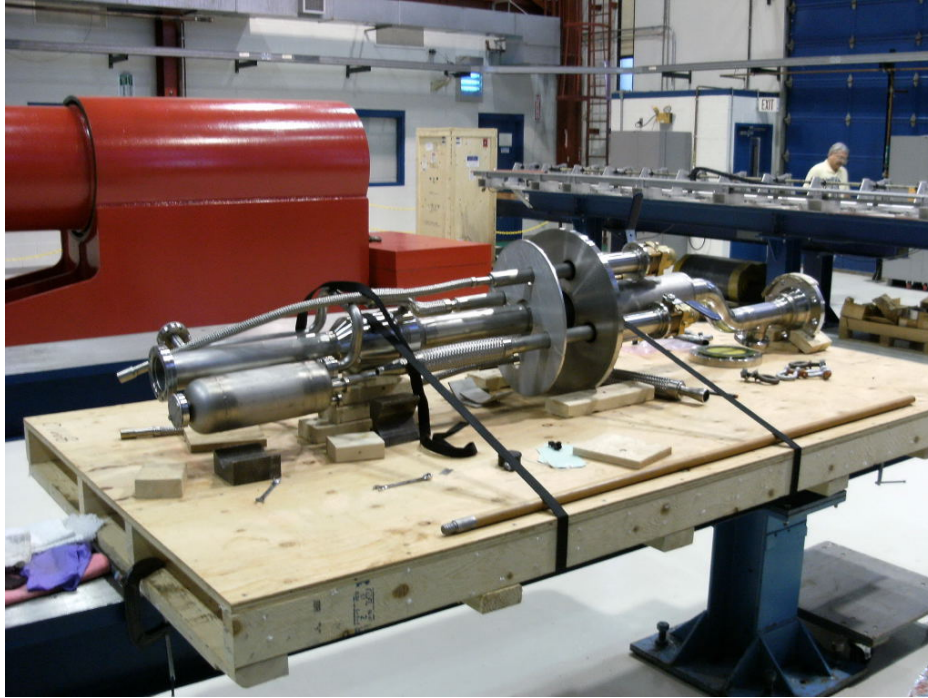

Fig. IV.4. Test cryostat LHe piping assembly; the phase separator is at lower left.

During the cold power testing, this LHe flow arrangement was suspected of introducing thermo-acoustic oscillations that made stable operation difficult.   In particular, this arrangement effectively creates two connected volumes of helium at different pressures (the phase separator volume, and the current lead volume) that cause helium to slosh through the magnet between them. This difficulty was eventually overcome as a stable operating point was found. However, this situation led to reconsideration of the internal piping design for production cryomodules.

V. Test Stand and Operation

Stand 4 in the Magnet Test Facility was adapted to provide the mechanical support and cryogenic services to the Test Cryostat. The cryostat was positioned as far North as possible on stand 4, to limit transfer line and cable lengths, with the constraints imposed by the LHC feedbox, and the need to open the North cryostat end dome.   Three new long flexible transfer lines were designed, built, reviewed for safety, and pressure tested: one to supply liquid nitrogen to thermal shields, one helium supply, and one helium return line. The notion is that any future Test Cryostats (e.g., for study of solenoid alignment) could be supplied by these same transfer lines, by arranging to have the top hat positioned in the same location.

Before placing the cryostat on the stand, the current lead assembly was mounted and spliced to the magnets. After checking the electrical circuits and instrumentation, warm Hall probe calibration measurements were taken. The Test Cryostat was then mounted on Stand 4 and connected to the MTF cryogenic systems using the three new transfer lines. Fig. V.1 shows the cryostat assembled with the current leads and the Hall probe panel. In Fig. V.2 the cryostat is connected to LHe supply and prepared for cooling down and powering. Roughing and Turbo pumps to evacuate the vacuum vessel were placed at the South end of the vessel, to keep them out of the congested instrumentation area during the test.
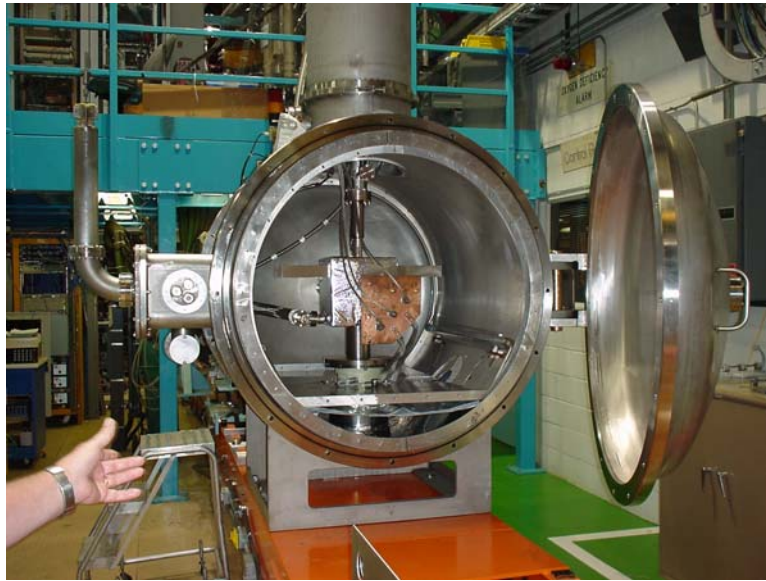

Fig. V.1. Bare Test Cryostat mounted on Test Stand 4 during preparation for cold test, prior to end thermal and magnetic shielding installation, and electrical connections.
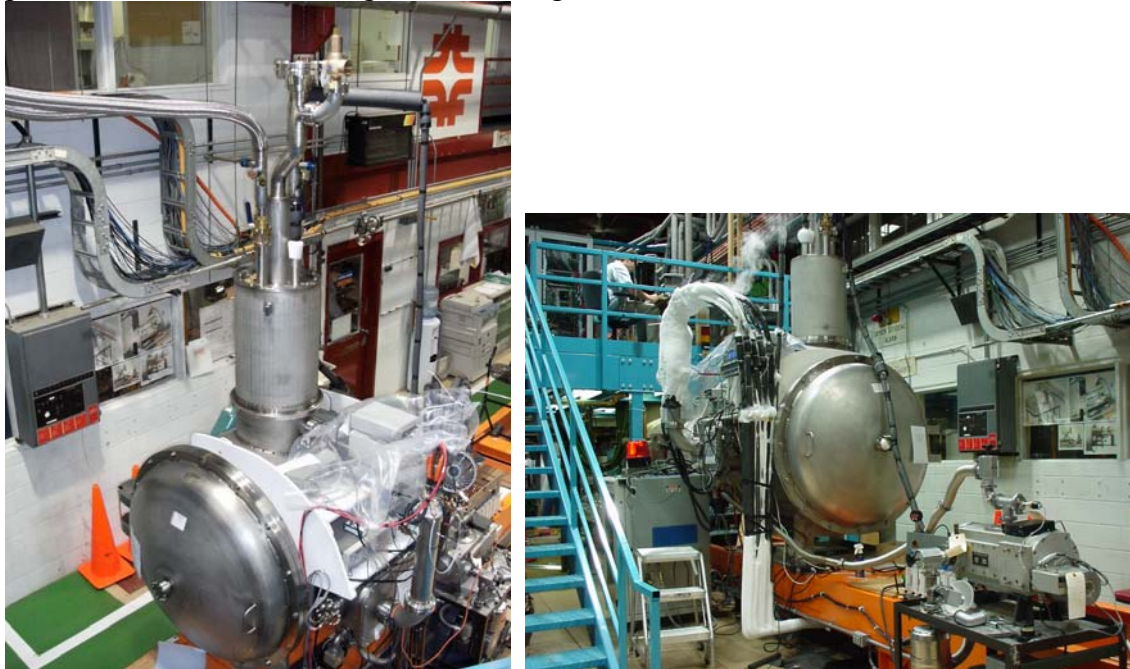

Fig. V.2. Test Cryostat connected to cryogenic supply and return lines and prepared for taking measurements.

Cryogenic Instrumentation

The Test Cryostat was instrumented with Cernox and Platinum Resistive Thermal Detectors (RTDs) in order to monitor temperatures of liquid helium and thermal shields. A liquid level (LL) probe was installed into the phase separator in the piping assembly (see Fig. IV.4), and two Cernox RTDs were mounted at the bottom end of the LL probe; these were the only sensors available to measure the temperature within the cryogenic subsystem. No temperature sensors were installed on the solenoid cold mass or the helium vessel: the test experience has shown that such sensors would have been very useful during the test to understand the erratic quench performance and actual cryogenic conditions early in the test.

Cryogenic scheme description

The hydraulic scheme of the system is documented in the drawing number 1670-ME-418332, which is stored in the folder Q:\TDarchivedDrawings\drawings on the TD Server1. An intuitive schematic view of the piping and instrumentation layout is captured by the cryogenic operator control system interface, which is shown in Fig. V.3. The valve and instrument list is available as a T&I document, TID-N-64, which is located on the web at http://tiweb.fnal.gov/website/controller/545.
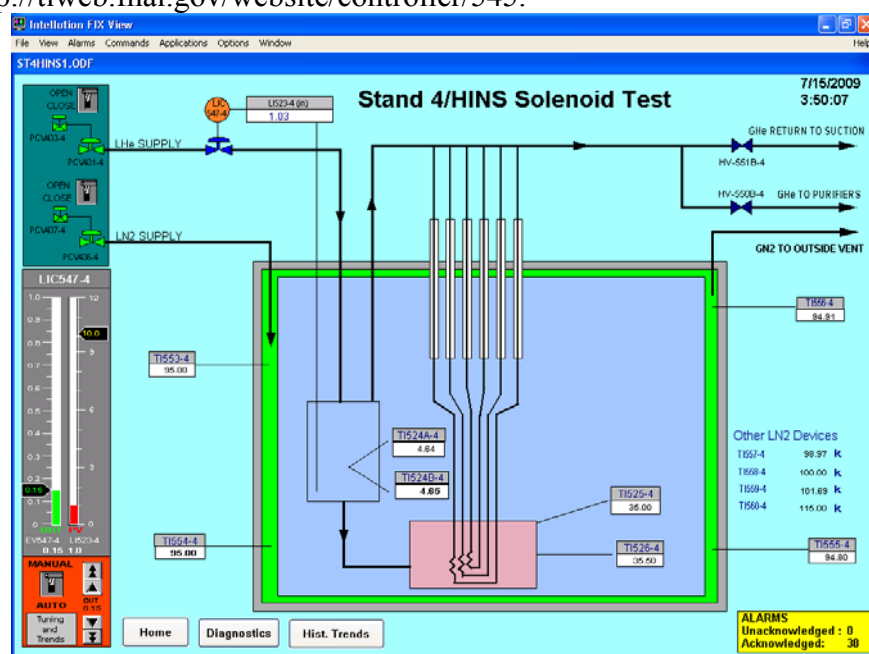

Fig V.3. Test Cryostat Flow Schematic as depicted in the Cryogenic Operator Interface.

The liquid helium is supplied to a phase separator inside of the test cryostat via a vacuum jacketed flexible transfer line. To control the helium flow, a cryogenic control valve is installed in the transfer line. At the phase separator liquid helium was sent to the solenoid vessel. Gaseous helium was vented via six conventional current leads and then combined with the vapor helium return from the phase separator. Helium flows from the individual return lines were warmed in copper heat exchangers, and were monitored and controlled via (40 scfh) roto-meters.

Liquid nitrogen was also supplied from the cryogenic distribution box via a flexible transfer line. The nitrogen supply line had no control valve to control its flow,

but the supply valve on the distribution box allowed some N2 flow adjustment. The LN2 supply temperature during the test was approximately 95 K, which is governed by the pressure in the IB1 LN2 distribution system; shields were slightly warmer (see Fig. V.4).

Test Operations

In early July the system was pumped down to the level of 10^{-6} Torr (at the pump) and no helium leak was observed. The first attempt to cool down was on July 8, and initial powered operation of the solenoid gave confusing results: quench performance was erratic and at levels well below the expected quench current. The liquid level probe and temperature sensors seemed to indicate that thermo-acoustic oscillations were taking place, and suggested that the solenoid was not immersed in a stable bath of liquid helium. The cool down and operating procedures had been developed prior to the test, and improved as the test progressed and engineers determined how to achieve a stable operating mode (the operating procedure is available as a T&I department document on the web at http://tiweb.fnal.gov/website/controller/1208). Therefore, early magnetic measurement studies were done at relatively low current (150 A and below).

Once stable conditions could be reproduced, systematic measurements were made for each Hall probe. Since data for only one probe could be recorded at a time, and points were needed at multiple currents, the data taking took several weeks to complete. The test was basically finished in time for a scheduled power outage that forced the cryogenic and data taking systems down from July 24 to 28. During this time, some useful upgrades to the Hall probe readout were made, and another set of magnetic measurements was captured, extending over a wider range of magnet currents for a subset of the probes. The cold test resumed on August 5 and was completed on August 8, after which components were warmed up. The best cryogenic system performance and Hall probe data quality were obtained during this final week of operation.   Some representative plots of conditions during this last week of operation are shown in Figures V.4 – V.6, respectively showing the thermal shield temperatures, the helium and magnetic shield temperatures, and the magnet current during testing on August 6.
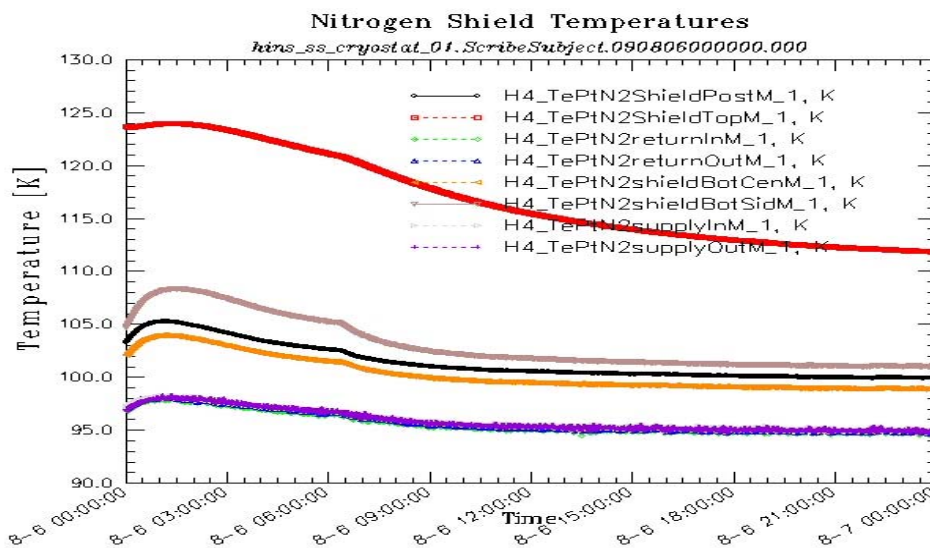

Fig. V.4. Thermal shield temperatures at various locations within the SSR Test Cryostat.
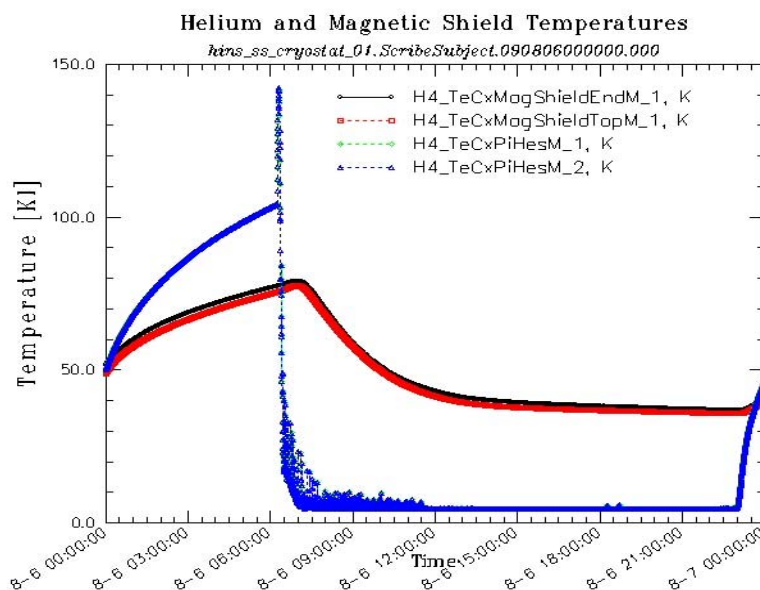
Fig. V.5. Helium and Magnetic Shield temperatures, showing a daily cycle and approach to stable conditions needed for powering the solenoid.

The long thermalization time of the magnetic shield, about 4-6 hours, indicates that the thermal conductance from the LHe vessel to the shield is not adequate. As a result, design of the pre-production focusing solenoid magnetic shield was significantly changed to improve its thermal properties.
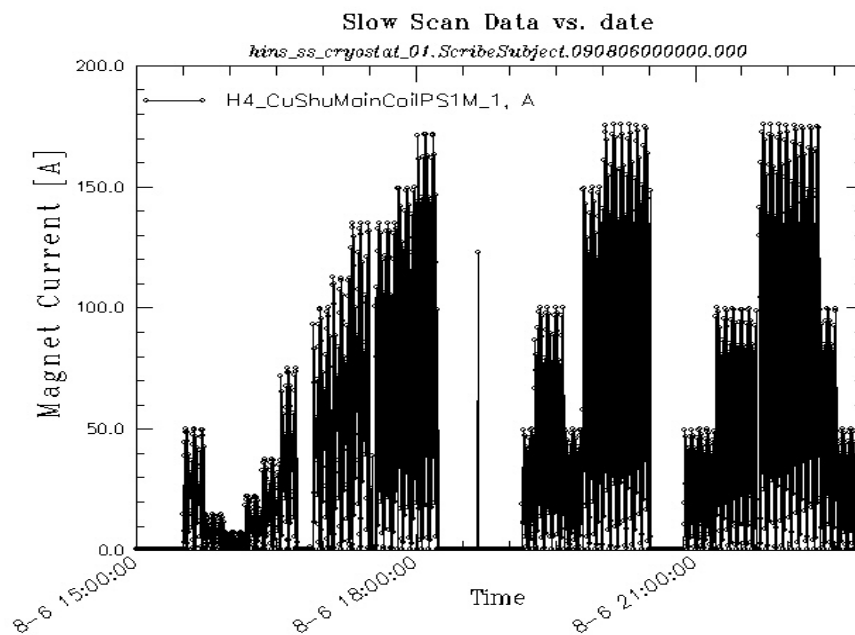

Fig. V.6. Magnet Current ramps for testing of Hall probes at numerous current levels.

VI. Magnetic Measurements

Hall Probe Array

The magnetic studies were carried out using an array of eight cryogenic Hall probes, commercially available from Cryomagnetics, Inc., mounted on a copper plate. The nominal DC drive current is 100 mA, and with a probe resistance of 1 Ohm this results in 10 mW of heat generation. To provide a better heat sink to the Hall probes, and to the associated probe coils, the plate was made of 2 mm thick copper with the probes and the coils installed as shown in Fig. VI.1. The plate was connected to the LN2 shield of the cryostat using two copper braid straps with a total copper cross-section of ~50 mm^2. The temperature of the plate was about 100 K, as measured by a Cernox RTD (X50630) attached near the copper plate center.
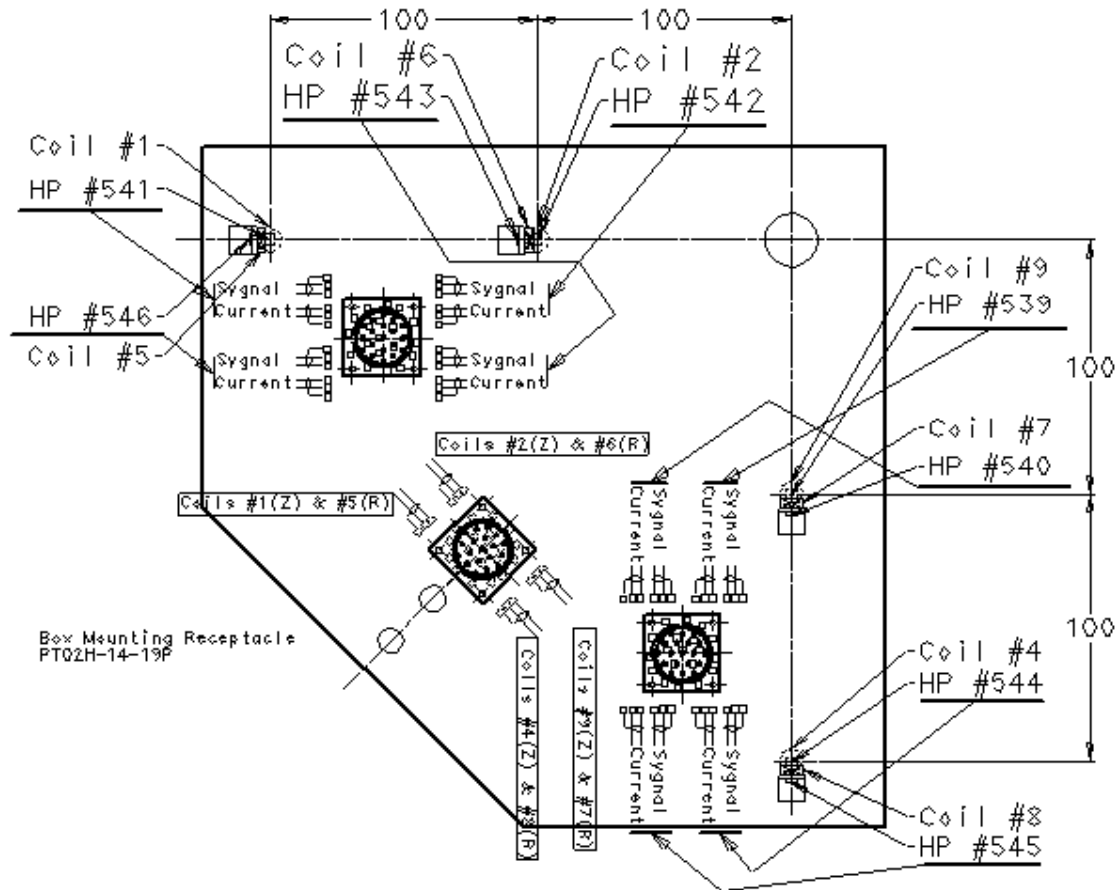

Fig. VI.1. Hall probe panel layout as viewed from the solenoid.

The Hall probes were installed on the plate to measure longitudinal (Z) and radial (R) field components. They were positioned along both horizontal and vertical axes to characterize the 3D shielded fringe field. Each Hall probe was coupled with a small solenoidal test coil that was able to generate relatively strong field (~5 G at 100 mA), to be able to check integrity of the Hall wiring and calibrate the probe response and system noise levels at different stages of the test. Each coil was wound on an aluminum spool using #36 ML insulated copper wire (~1 cm diameter, 100 turns in each coil). Each pair

of coils, corresponding to a complementary (R,Z) pair of Hall probes, was connected in series in a way that increased the field at the location of each probe.
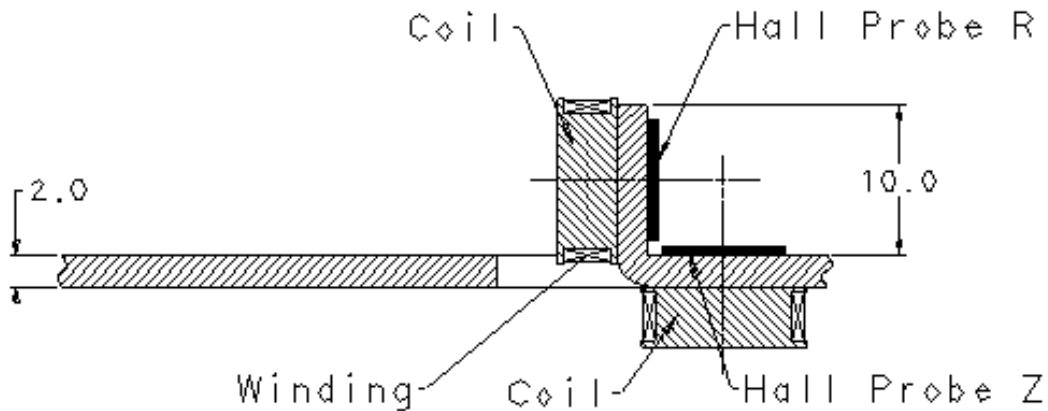

Fig. VI.2. Mounting scheme for the probes and the coils on the copper plate.

The plate was oriented in the plane perpendicular to the solenoid axis at the distance corresponding to the nearest wall of a SRF cavity, 225 mm from the solenoid center. Figure VI.2 shows a section through the copper plate illustrating the test coil and Hall probe mounting scheme. Each probe was placed so that its marked surface was oriented up from the corresponding mounting area of the plate; the Hall probes were not precisely centered with respect to the coils, but were typically within one or two millimeters of the center. The probes sensitive to the radial field are 5 mm closer to the solenoid than those oriented to measure the axial field. Fig. VI.3 shows a photo of the actual plate looking toward the solenoid. A final assembly photo was shown in Fig. V.1.
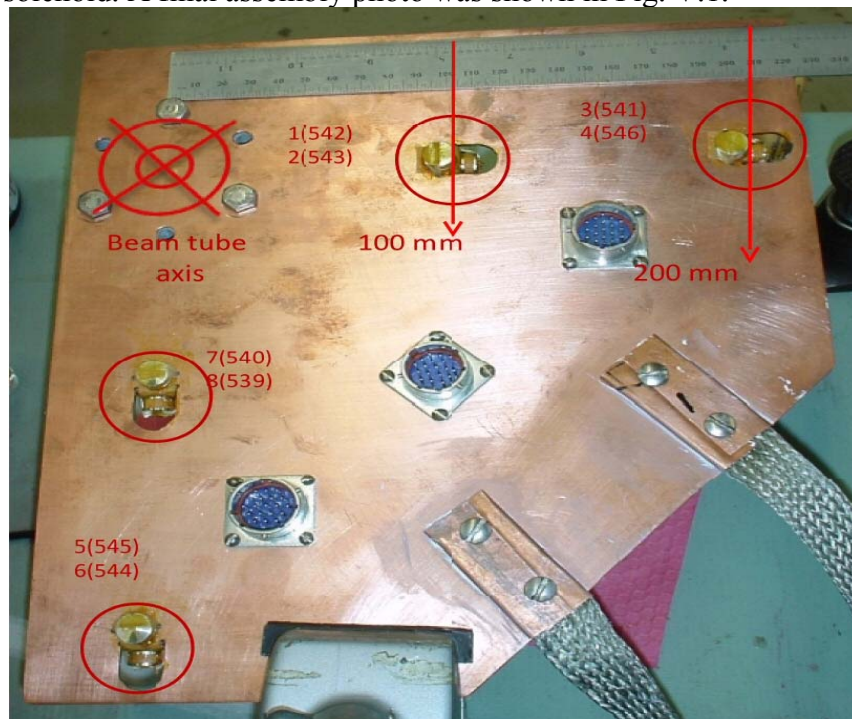

Fig. VI.3. Completed Hall probe panel; the view facing towards the solenoid.

Sensors and Readout System

HSP-T Hall probes by Cryomagnetics, Inc. were used. The probes were calibrated at Cryomagnetics, Inc. at 300 K. The corresponding sensitivities, which are expected to be the same within about 1% at cryogenic temperatures, are shown below in Table 1 for a 100 mA excitation current.

Table 1: Hall probe sensitivities

Probe #	539	540	541	542	543	544	545	546
Sensitivity (mV/T)	34.9	31.5	61.8	40.3	36.0	28.7	24.2	45.0

Because the spread in sensitivity is quite large, the probes were sorted to work in pairs to measure the Z and R components of the stray field in four locations: two in the horizontal plane and two in the vertical plane, at R = 100 mm and R = 200 mm. The pairs were chosen to have close sensitivities, as indicated in Table 2.

Table 2: Hall probe placing

Radius	R = 100 mm		R = 200 mm	
Orientation: Plane:	Longitudinal	Radial	Longitudinal	Radial
Horizontal	#542	#543	#541	#546
Vertical	#539	#540	#544	#545

Three nineteen-pin connectors were used to complete wiring of the Hall probe plate, and three cables with twisted and shielded pairs were used to connect the plate connectors to those installed on the cryostat. Two connector pins for excitation and two for voltage measurement were allocated to each Hall probe; the pair of test coils for each (R, Z) probe pair required the use of two additional pins. Based on the sensitivities in Table 1, the expected voltage signal from the Hall probes at 10 µT is about 0.3 µV. Therefore using twisted and shielded pairs is a necessary measure to reduce inevitable noise. The probes were connected to a current source by using twisted and shielded pairs, and similar wiring arrangements were made to read the Hall voltage signal and power the test coils. Wire lengths were kept as short as possible for noise reduction by mounting electronics adjacent to the Test Cryostat connector flange (on shelving in Fig. V.2).

The solenoid and test coils were (separately) excited with low frequency (10-30 mHz) sinusoidal current waveforms, in order to correlate the current and field signals. Two readout techniques were employed during the test. In the first technique, (Fig. VI.4), a low noise DC-current source was used to excite the Hall probe, and the Hall voltage was digitized with a DVM. In the second (Fig. VI.5 and Figures VI.6a and VI.6b), a lock-in amplifier provided an AC reference voltage which generated an excitation current via a transformer (for impedance matching and amplification); the Hall voltage was then sampled by the lock-in amplifier which output both in-phase and out-of-phase amplitudes. In both DC and AC methods, the Hall voltage was routed through a low-

noise pre-amplifier and low-pass filter prior to digitization at a sampling rate of 240 Hz. Table 3 lists the specific instruments used for the magnetic measurements.

Table 3. Instrument List for Low Field Magnetic Measurements

Function	Instrument	Serial No.	AC/DC	Comments
Signal Generator	Agilent 33120A	N/A	AC, DC test coil excitation	5V, 30 mHz
Current Source	EDC520A E-series	15597	DC, Hall probe excitation	+/- 100 mA
Pre-Amp 1	SRS SIM911 BJT Pre-Amp	5883	AC, DC	
Pre-Amp 2	Signal Recovery 5113	9175934	AC	Battery Powered
Low-Pass Filter	SRS SIM965 Analog Filter	6918	AC, DC	20 Hz cutoff Butterfield DC-coupled
Digitizing Voltmeter	PXI-6281 multi-Function DAQ	191501C-03	AC, DC	240 Hz sampling rate
Lock-in Amplifier	Signal Recovery 7265 DSP	699	AC	

These devices were all controlled and read out using LabView programs, connected through a PXI crate via a fiber optic link (for ground isolation) and running on a Windows PC. Data were collected by a LabView program that used pre-built data-acquisition block and data-saving block, so the data are in "standard" LabView "measurement file" (.lvm) ASCII format. A file has about 24 lines header and collected data in a few columns. The LabView readout programs are archived on the tdserver1 project drive in the folder:
Q:\8GeVLinac\PD Magnets\StrayFieldMeasurements\SSR1_TestCryostat\Programs
Each file contains data for a single measurement "point," i.e., a time-series taken from a single Hall probe with fixed measurement parameters like the Hall excitation current, magnet drive amplitude and frequency, etc. The file name consist of a prefix that usually indicates whether the data represent test-coil calibration, which Hall probe is being measured, etc., the date and time stamp (with minute accuracy), and a suffix which is just an incremental number starting from -01. Data files collected in a single day were arranged in a separate directory, whose name contains the date when the data were taken. Each such directory contains a file with name like 00readme.txt that has a short description of the data files there. The raw data files are archived on the tdserver1 project drive, as 'zipped' files in the folder:
Q:\8GeVLinac\PD Magnets\StrayFieldMeasurements\data_archive.
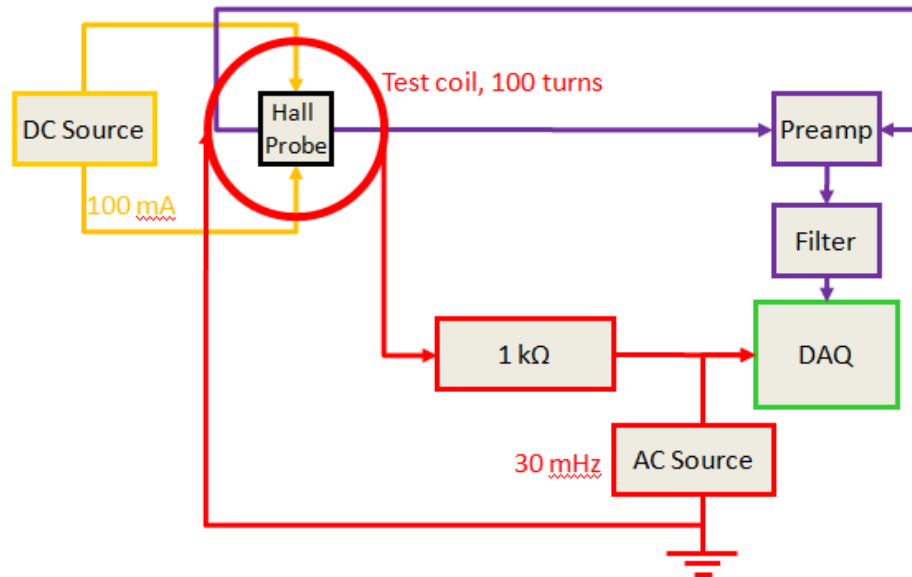
Fig. VI.4. DC probe excitation setup. The probe was excited by a constant 100 mA (positive and negative polarities). The Hall probe signal was conditioned by a BJT preamp (x100 gain) and a low-pass filter. The test coil was driven at 30 mHz to simulate the solenoid's ramp profile. The 1 kΩ resistor allowed the test coil current measurement. Solenoid DC scheme was similar, but with solenoid rather than test coil as source of magnetic field, and different current reference signal.
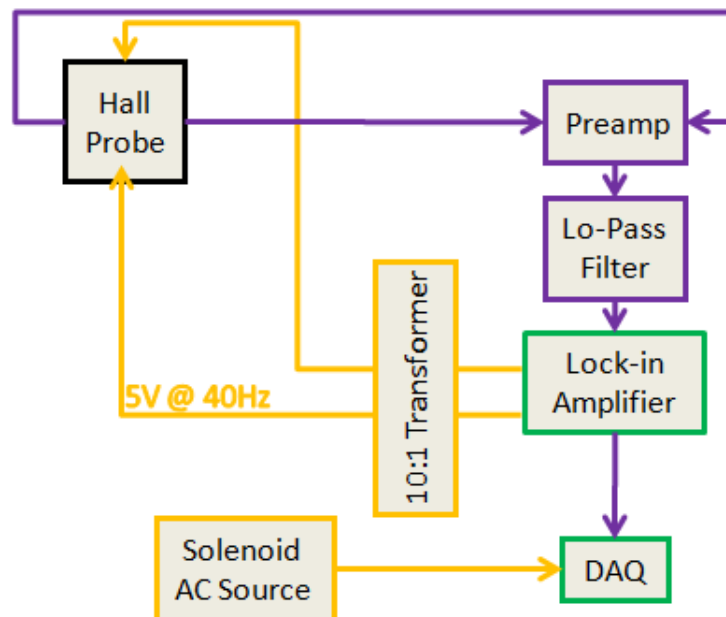

Fig. VI.5. Schematic of the original cold measurement setup. The data acquisition system recorded both lock-in amplifier outputs and the solenoid power supply signal. The lock-in amplifier drives the probe with 5 V_{AC} at 40 Hz, to avoid 60-cycle noise. The probe signal is amplified and conditioned before being processed by the lock-in amplifier.
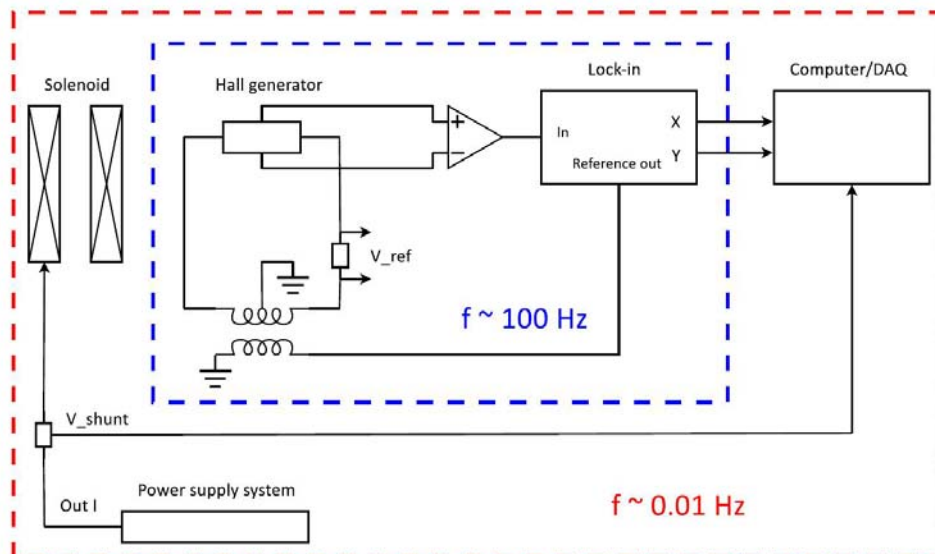
Fig. VI.6a. The second cold AC measurement setup, for which the transformer was changed and a precision shunt resistor (1.8195 Ω) added to monitor the Hall probe current during the second set of measurements, which used a 4 V_{RMS} at 150 Hz Reference Out drive signal from the lock-in amplifier. See also Fig. VI.6b.
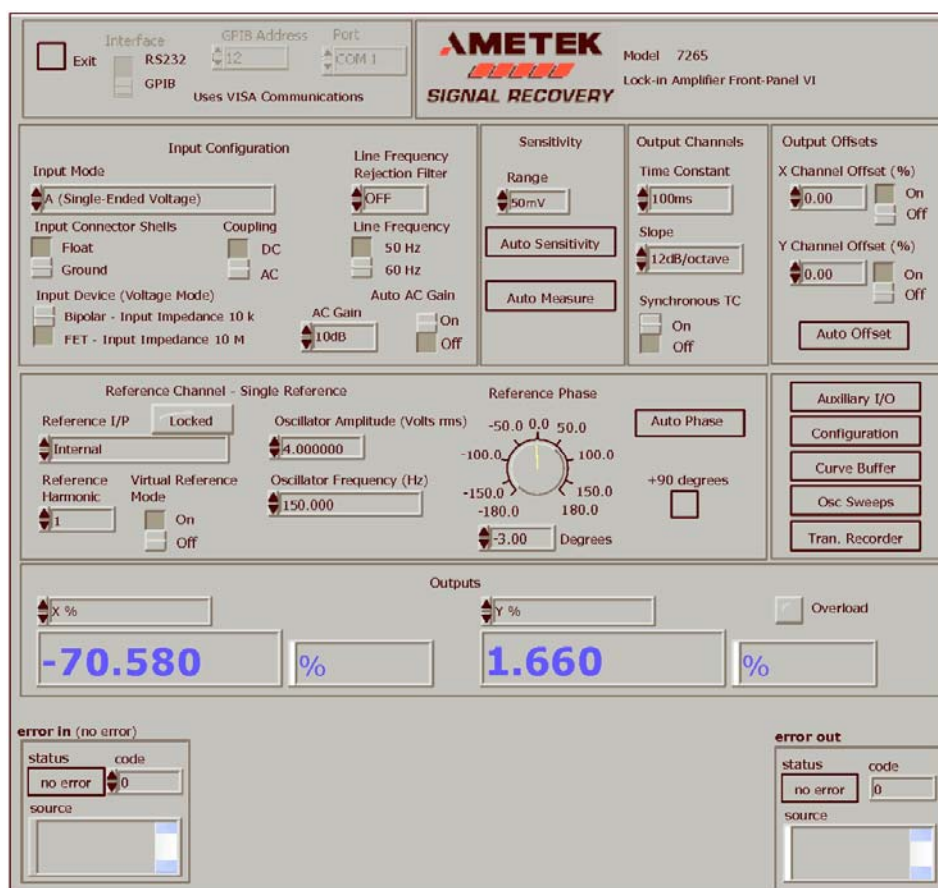

Fig. VI.6b. Screen capture of the Labview lock-in amplifier control interface, illustrating all "fast loop" control parameters used during the solenoid AC test.

The Measurements

After the solenoid and shield were mounted and the assembly was fully connected and leak checked in the test cryostat, the first set of magnetic measurements was made at room temperature to check that all probes and test coils worked as expected, and to capture calibration (probe sensitivities) and noise level information for both DC and AC techniques. Similar test coil measurements were made after cool down to 4.6 K, to verify that no failures had occurred from the change in thermal conditions. Subsequent studies with the powered solenoid revealed that noise level introduced by the power supplies was unacceptably high: the signal was several orders of magnitude below the noise. The following steps were taken to reduce noise level:

- AC power was conditioned using a Sola isolation transformer to power all of the data acquisition electronics.
- To reduce noise introduced by the solenoid power supply, all electronic devices were isolated from IB1 ground and AC power by using a battery-powered UPS unit.
- A battery-powered pre-amplifier was tried to provide more isolation.
- The power supply ground point was changed in several configurations.

Because these measures did not result in the desired noise level reduction, we were forced to switch to AC measurement technique.

The AC technique was very successful in digging a signal out of the noise, and all probes showed good correlation of the in-phase signal with solenoid (or test coil) current. Adjustment of the Lock-in phase and stability for each probe was studied using the test coils: some slight but essentially negligible phase variation between probes is thought to arise from small differences in wire lengths and stray inductance or capacitance. There was initially some uncertainty about how to interpret the signal amplitude – for example, whether the Lock-in amplitude reflects the "peak-to-peak" or "RMS" amplitude; this was determined by directly inputting the (measured) the lock-in waveform and observing the result. Comparison of the DC and AC responses using the test coils was also a useful as a way to understand that the AC signal made sense, and this correlation is shown in Fig. VI.7. The AC technique was therefore utilized for all of the cold solenoid measurements.
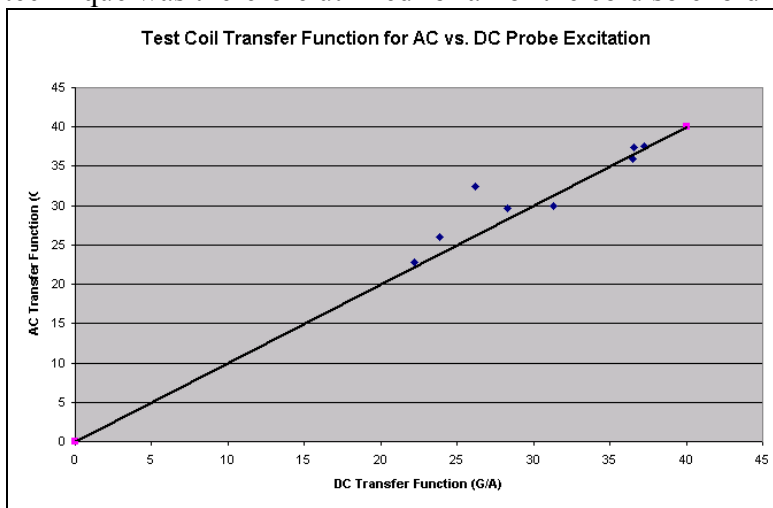

Fig. VI.7. Comparison of test coil transfer functions measured by AC and DC probe excitation of the Hall probes (one point per probe; line corresponds to the ideal case of perfect matching).

AC data were taken in two sets, from July 14 to 23, and again from August 5 to 8. In the first set, the Hall probe AC excitation current was not explicitly measured, but was calculated based upon the known Hall probe resistance, lock-in amplifier amplitude, and measured transformer ratio at the operating frequency of 40 Hz. In the second set, a specially designed matching transformer was introduced to increase the current through the Hall probe to improve the probe's sensitivity. A precision shunt resistor (1.8195 Ω) was put in series to measure the actual Hall probe current. The first set of solenoid magnetic measurements were taken with sinusoidal current ramps at 30 mHz and maximum amplitudes of 100 and 175 A. Achieving higher currents consistently was difficult due to cryogenic instability, and to avoid quenching and losing time the upper current was restricted to 175 A. Data were captured for a subset of probes at lower peak currents in the first data set. In the second set of data, a wider range of maximum solenoid currents was explored for five of the eight probes, to study the linearity of the measured fields. As will be seen, these data sets agree very well.

Analysis

The DC-excitation technique was studied as a function of the current amplitude (test coil field excited with a signal generator operating with 5 V amplitude at 30 mHz AC). Figure VI.8 shows the correlation and simple linear fit of Hall probe voltage as a function of the test coil current, as measured across the shunt resistor; many AC cycles are overlaid, and the noise level is evident. A series of such measurements were made for each probe, in which the test coil current amplitude was systematically reduced to estimate the accuracy for small signal detection using the simple linear fit. Fig. VI.9 shows an example of this, where the signal amplitude is accurate to better than 10% down to the level of about 2 μT.
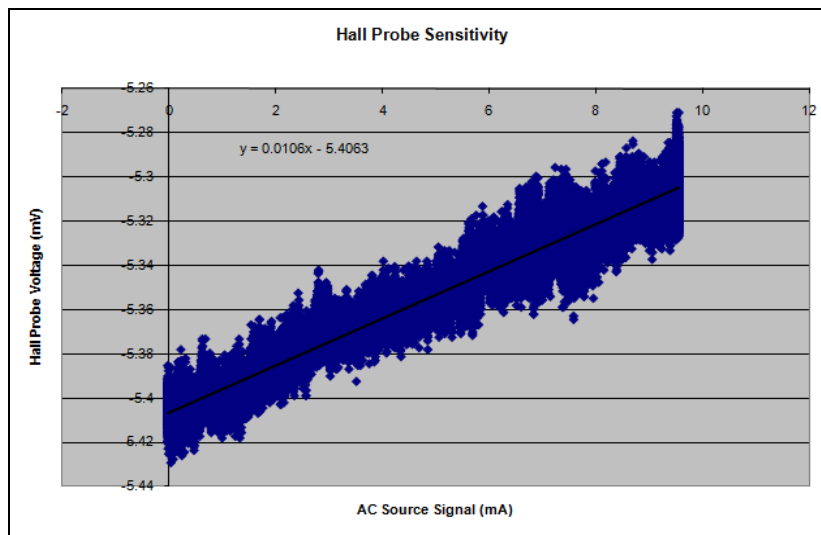

Fig. VI.8. Hall probe data correlation fit. This particular plot shows the behavior of probe no. 542 at 5 V_{AC} test coil excitation level, which corresponds to a nominal magnetic field of around 0.24 G (although two coils contribute - see Fig. VI.2).
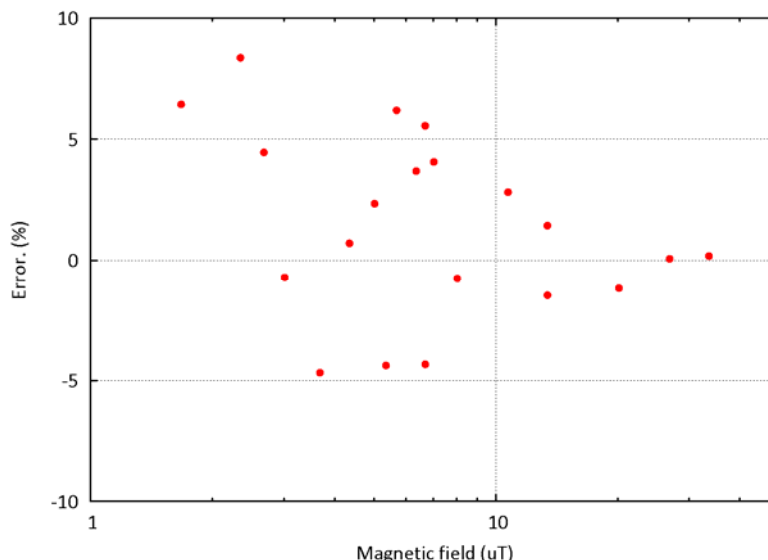
Fig. VI.9. Error in the Hall probe "DC sensitivity" measurement (with respect to the highest field value) versus magnetic field strength (note log scale). The plot shows data for one probe, but is typical.

The main idea of the AC technique is to drive the solenoid with oscillating current (at a fairly low frequency, so not to exceed dI/dt related thresholds) and look at the same frequency component in the signal from the Hall's sensors. Since expected frequency range is about 10 to 30 mHz, this procedure can be done in software (a "slow loop" phase-lock technique, on top of the fast hardware phase-lock loop). A separate program does a **generalized linear fit** to the amplified and digitized Hall probe signal data, to a function A*sin(ωt) + B*cos(ωt) +C , where A, B and C are fit parameters, and ω is a known frequency. In our test, the computer uploads a single-period-sine-wave current profile to the current source, the profile is then run in a continuous cycle. The actual current is recorded along with the Hall's signal. This record of the current is analyzed to establish the actual frequency. Examples of the Hall probe sinusoidal wave forms from the solenoid field are shown in Figures VI.10 and VI.11.

First, the drive frequency is determined by non-linear fitting to the drive voltage (test coil) or solenoid current data set. The issue here is that the power supply is driven by software and there is no guarantee that the actual frequency is what was programmed. (We pick the maximum amplitude harmonic component, which was typically 100 times greater amplitude than the next highest term). To do the fitting we use the program **harminv** (http://ab-initio.mit.edu/wiki/index.php/Harminv). Once the frequency was established, a simple Octave (~Matlab-ish) program did the linear fit to Hall probe data. In this "slow loop" analysis, we report only the magnitude of the signal vector, SQRT(A^2+B^2), essentially ignoring the phase information between the Hall probe signal and solenoid driven field. This could be included in the analysis, to improve the noise level by ~sqrt(2), if we are interested to push the technique in the future.

To determine possible contributions from noise to the AC signal at zero solenoid current, similar fits were made to the data, but with ω made to vary from the actual measured value. This kind of analysis revealed that the offsets are quite small.

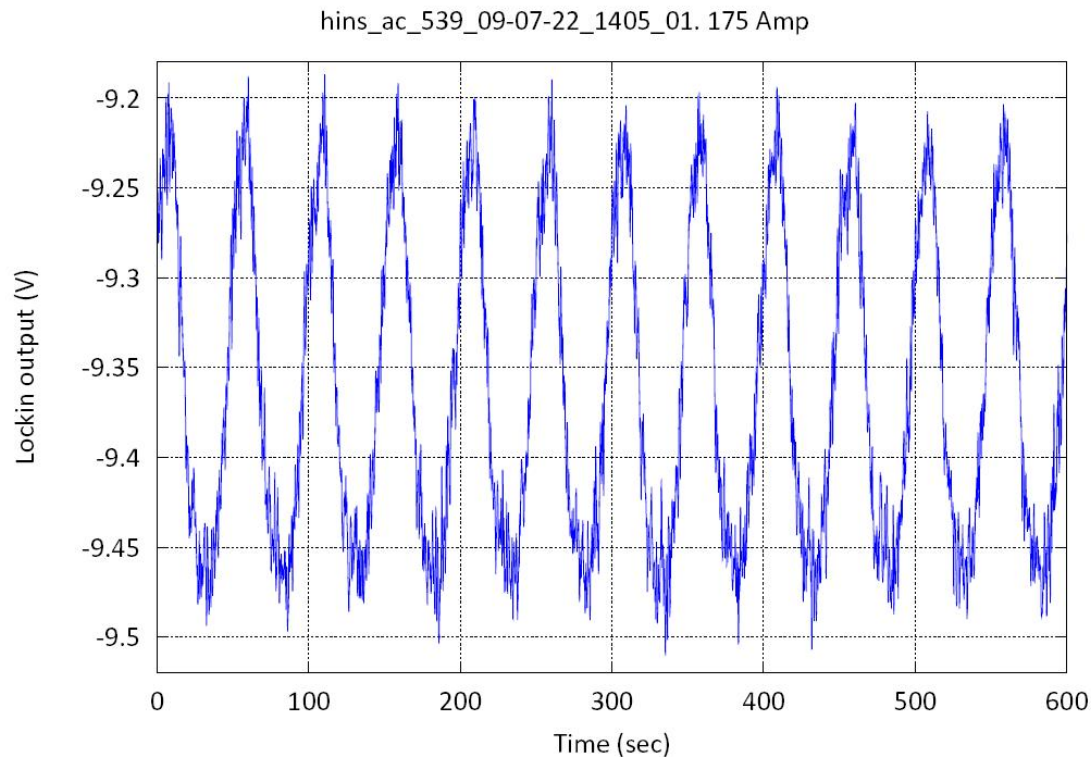hins_ac_539_09-07-22_1405_01. 175 Amp

Fig. VI.10. Probe no. 539 signal captured by lock-in amplifier as a function of time, which correlates well with the sinusoidal ramp profile used to drive the solenoid to 175A.
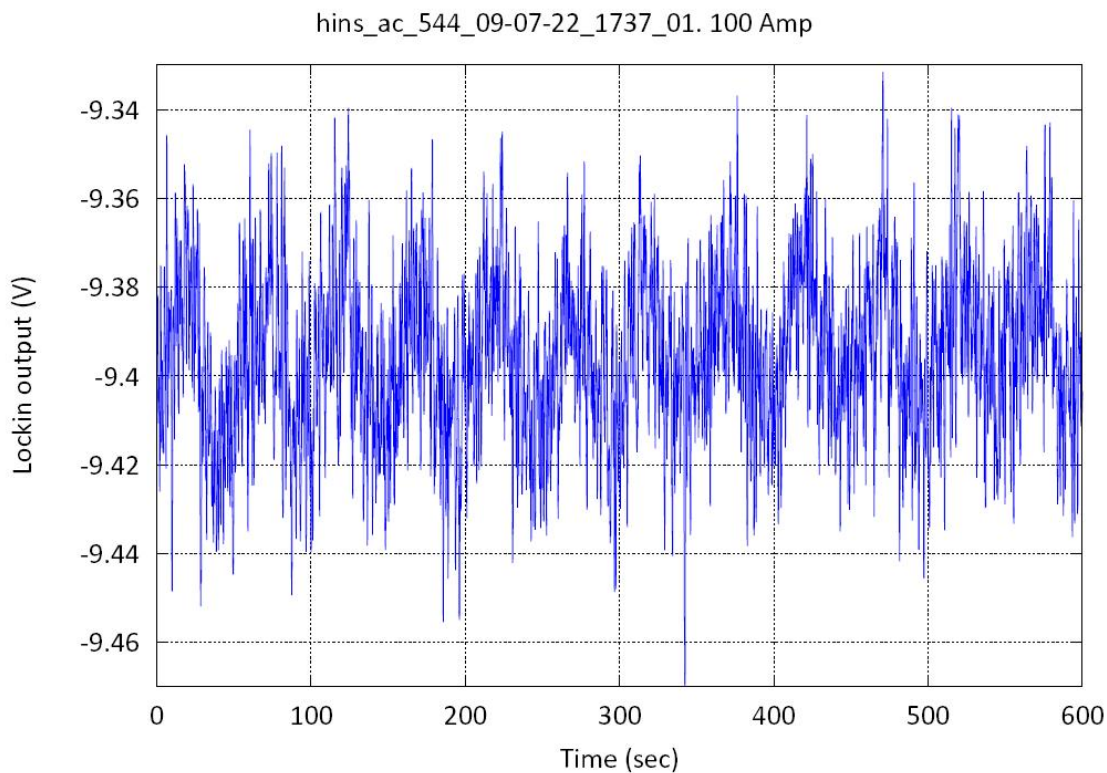
hins_ac_544_09-07-22_1737_01. 100 Amp

Fig. VI.11. Lower sensitivity probe no. 544 signal captured by lock-in amplifier as a function of time, for a sequence of solenoid sinusoidal current ramps to 100 A.

Test coils with AC excitation were used either before or after each solenoid measurement run, to check the fitting procedure and to verify linearity of the signal with excitation field. However, these were shorter runs than had been taken with DC test coil measurements (Fig. VI.9), and with fewer points in test coil amplitude. These showed a linear response with amplitude.

Results

Figure VI.10 is a plot of Hall probe field versus solenoid maximum current for all probes, taken during the first set of measurements. Lines are extrapolated to zero show the level of scatter in offset values. Error bars placed on the points are estimated from the (DC) sensitivity study shown in Fig. VI.9, and appear to be consistent with this level of scatter. Fig. VI.11 is an overlay of results from all of the probes which had data taken in both sets, with the same lines from the previous figure – showing that both data sets agree well. Figure VI.12 shows the second set data points plotted in a different way, with a line extending from zero, and possibly suggesting deviations from linear behavior at lower solenoid currents and field strength. Given the expected level of errors, it does not make much sense to try to interpret deviations from a linear extrapolation from zero. However, if this is real, one possible explanation could be the field-dependence of the iron yoke (flux return) material permeability.

Given this, finally we show in Fig. VI.13 and Fig. VI.14 the bottom line plots of magnetic field (Bz and Br components at 175 A solenoid excitation current) versus position, with overlay of model predictions. The agreement with the prediction is quite good.
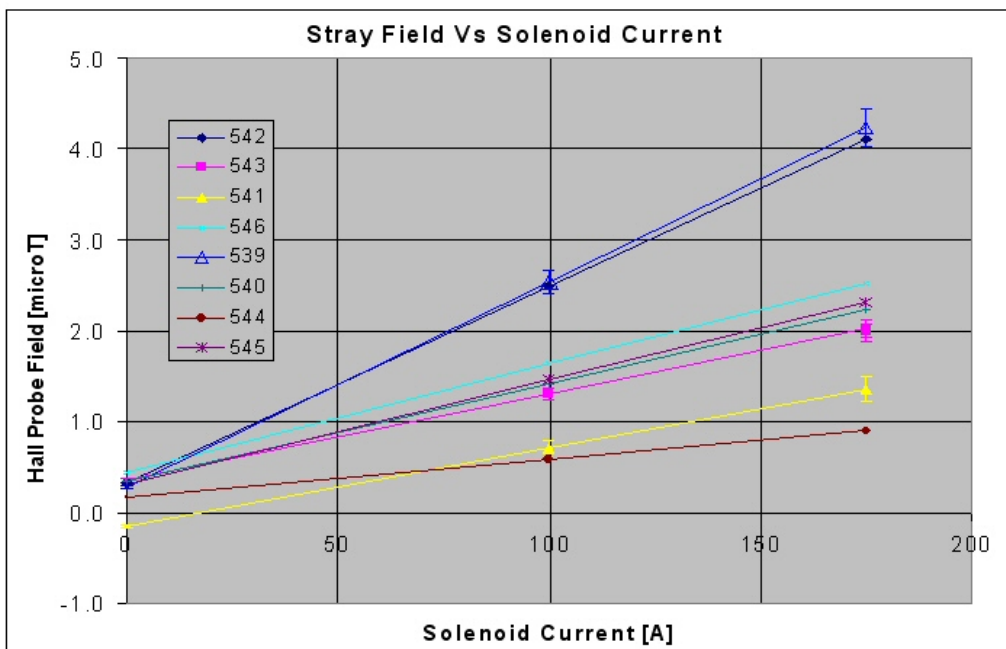

Fig. VI.10. Data from first set of measurements for all probes at 100 and 175 A. Lines are extrapolation through these two points for each probe, which show offset level at I=0. Error bars shown are 5 % for probes 542 and 543, and 10 % for probe 541.
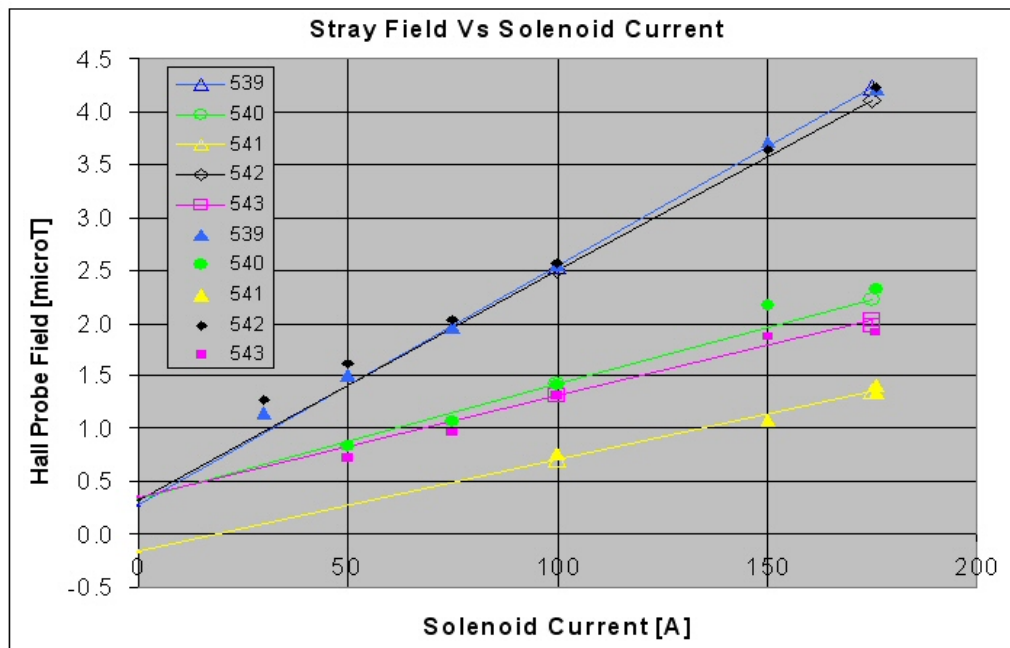
Fig. VI.11. Data overlayed from those probes where data were captured in both the first set (open symbols with line) and second set (filled symbols).
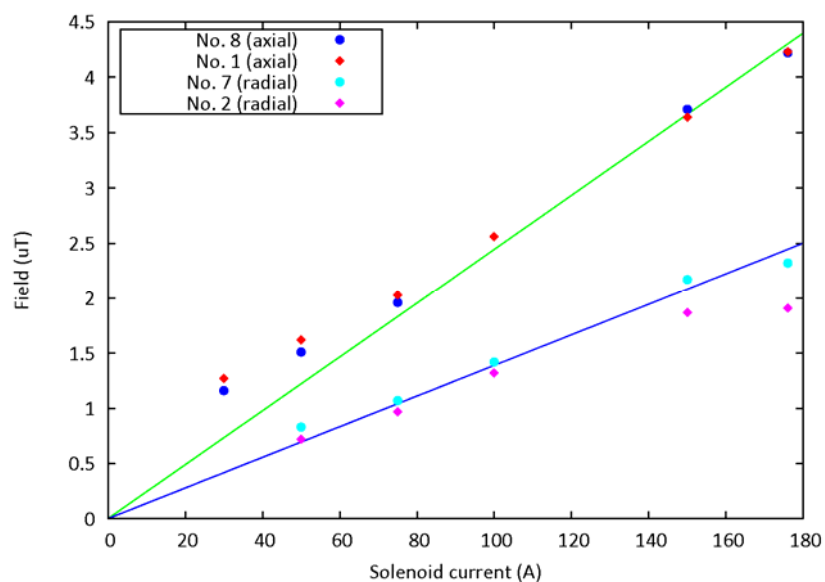

Fig. VI.12. Data from the second set of probes with wider current range, and line from zero to guide the eye.
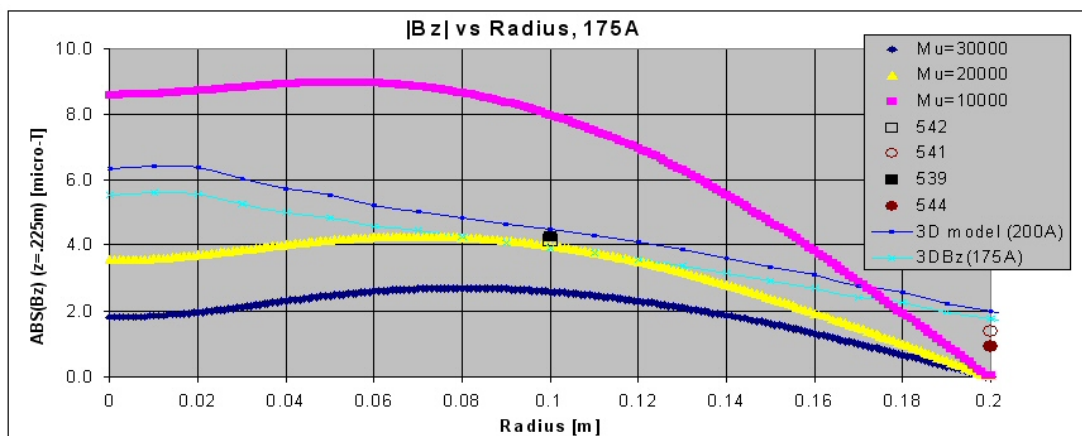
Fig. VI.13. 2D (varied μ) and 3D (μ=10000) model predictions for Bz versus radial distance from the axis, with overlay of 175 A data from probes in both horizontal and vertical axes.

Fig. VI.14. 2D (varied μ) and 3D (μ=10000) model predictions for Br versus radial distance from the axis, with overlay of 175 A data from probes in both horizontal and vertical axes.

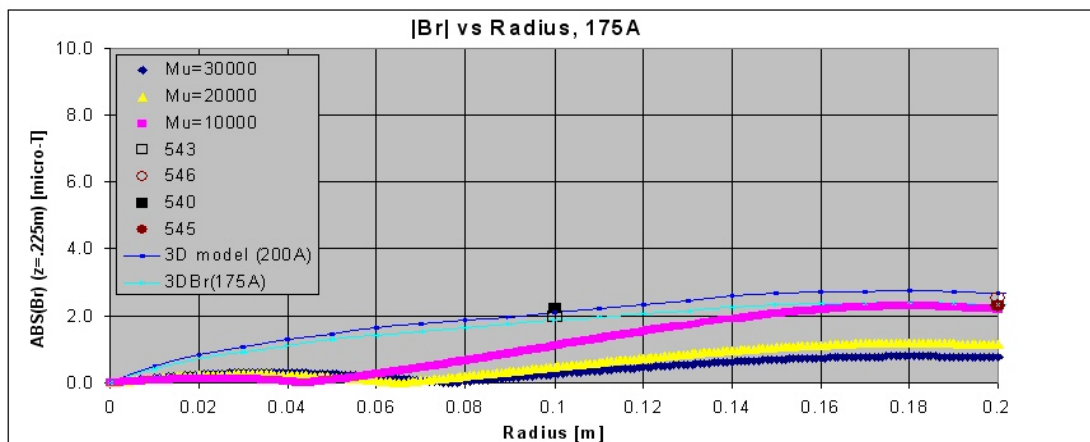**Conclusions**

To verify the effectiveness of the magnetic shielding of solenoid-based focusing lenses, a direct set of measurements was made at TD to measure the lens fringe field distribution at nominal current and in the environment close to what is expected in the production cryomodule.

To make the measurements possible, the test cryostat made for SRF cavity testing was modified to allow installation and powering of the prototype SS1 focusing lens. These modifications included building new cryogenic interface and adding a current lead assembly to the existing cryo-vessel.

The effectiveness of the cryostat magnetic shield was investigated by measurements without and with the shield to conclude that the shield does provide necessary degree of the earth magnetic field reduction.

Weak magnetic field measurement methods were developed to allow the fringe field measurements in vacuum and at low temperature environment. Corresponding equipment

set was assembled; needed instrumentation and shielded cabling was designed, built, and tested to work properly.

The cryostat and the test setup were assembled in IB-1 (test stand 4). The cryostat was cooled down; a cryo-acoustic instability was found to be a possible danger for future production cryomodules. To avoid it, different position of the current lead assembly needs to be considered. A way to stabilize the situation was found and implemented which allowed futher measurement sessions.

The DC fringe field measurement method was shown difficult to use due to the noise from the solenoid current supplies. If more detailed (and lower field) measurements are needed in future, a set of power supplies with lower noise will be needed.

The AC fringe field measurement method was adequate to allow reliable field measurement down to below 10^{-6} T. The measurements from this experiment are in good agreement with the magnetic shield modeling prediction. This adds a lot of confidence to the modeling study, and allows further modification and optimization of the shield. One recognized improvement is the need to shield magnetic field from superconducting leads.

The data suggest there is a possibility of non-linear behavior at low magnet current, which could be the result of unknown magnetic properties of the cold iron yoke. Further investigation of this, measuring the effectiveness of a new SS1 pre-production shield design, as well as characterizing the performance of other (perhaps less expensive) low-temperature magnetic shielding materials, would be a natural path for continuation to this work.

By employing groups and specialists from several departments within the Technical Division, we completed successfully, and in a timely manner, this non-trivial and rather complicated study, while making additional findings and overcoming many difficulties along the way. The results are of great importance for future work towards designing and building a prototype version of a production cryomodule.

References:
1. T. Khabiboulline, I. Terechkine, "HINS Linac Front End Superconducting Cavity Magnetic Field Requirements," TD-08-006, FNAL, February 2008.
2. G. Davis, et al., "Pre-Production Solenoid for SS1 Section of HINS Linac," TD-09-010, FNAL, April 2009
3. T. Nicol, G. Lanfranco, L. Ristori, "High Intensity Neutrino Source Superconducting Spoke Resonator and Test Cryostat Design and Status," *IEEE Trans. Appl. Supercond.*, Vol. 19, No. 3, June 2009, pp1432-1435
4. G. Chalachidze, et al, "HINS_SS1_SOL_02d Fabrication Summary and Test Results," TD-09-001, FNAL, March 2009.
5. T. H. Nicol, et al, "Design and Analysis of the SSC Dipole Magnet Suspension System", *Supercollider 1*, Plenum Press, 1989, pp. 637-649.